Ⅲ. NHEと筋ジストロフィー

筋ジストロフィー(筋ジス)とは，筋線維の破壊・変性と再生を繰り返しながら，次第に筋萎縮と筋力低下が進行していく遺伝性筋疾患の総称である。発症年齢や遺伝形式，臨床的経過等から様々な病型に分類されるが，最も頻度の高いのはデュシェンヌ型筋ジストロフィー(DMD)であり，1987年に細胞骨格蛋白質であるジストロフィンがその原因遺伝子として特定された。DMD以外にも細胞骨格系蛋白質の異常に起因する筋ジスが数多く知られているが，未だ筋細胞変性の詳しい分子メカニズムは明らかでなく，良い治療法がないのが現状である。

著者らはジストロフィン欠損で筋ジスを発症するマウス(*mdx*)またはその関連蛋白質サルコグリカン欠損で筋ジスと心筋症を同時発症するハムスター(BIO14.6)をモデル動物として使用し，筋変性に効果的な薬の探索を行ってきた[17]。最近，NHEの阻害剤(カリポライドあるいはEIPA，化学構造は図4A参照)が筋変性に対して有効であることが分かってきた[18]。NHE阻害剤投与群では非投与群に比べて筋変性の指標となる血中クレアチンキナーゼ(CK)活性の有意な減少と組織ヘマトキシリン/エオジン染色で観察される筋変性の改善が認められた(図4B，C)。また，金網にマウスをぶらさがらせ，前足による体重支持時間を測定し，骨格筋の機能的評価(グリップテスト)を行ったところ，NHE阻害剤投与群において筋機能改善が示された(図4D)。このようなNHE阻害剤による筋変性の改善効果から，筋ジス筋ではNHEが活性化されており$[Na^+]_i$の上昇によって，前節で述べたようなNa^+依存性Ca^{2+}過負荷が起こり，筋変性が引き起こされる可能性が考えられた[18]。

そこで実際に筋ジス動物から調製した筋細胞を用いて，NHE阻害剤の筋変性保護メカニズムを検討した。筋細胞へのNa^+取り込み実験を行ったところ，全Na^+取り込みの大部分(65％以上)がNHEの特異的阻害剤で抑制されたことにより筋細胞におけるNa^+流入にNHEの寄与が大きいこと，そしてNHEを介する流入が筋ジス筋細胞で上昇していることが判明した。また筋ジス筋細胞では，コントロールに比べてpH_iの上昇，NHE活性のpH_i感受性の増加が観察された。$[Na^+]_i$も筋ジス筋細胞で約1.5倍上昇しており，カリポライド処理でコントロールレベルにまで減少した(図5A)。

以上の結果から，筋ジス筋細胞ではNHE活性が大幅に上昇していることが判明した。筋ジス筋細胞では外液Ca^{2+}濃度を上げるとコントロールでは観察されない$[Ca^{2+}]_i$の上昇が認められるが，この上昇はカリポライドであらかじめ処理することにより抑制され(図5B)，また同じ処理により伸展刺激による筋ジス筋細胞からのCK漏出も抑制された。この$[Ca^{2+}]_i$の上昇には強い外液Na^+濃度依存性があること，NCXブロッカーKB-R7943によって阻害されることから，筋ジス筋細胞ではNHEの恒常的な活性化による$[Na^+]_i$上昇がNCX活性を変化させることにより$[Ca^{2+}]_i$上昇をもたらし，筋変性につながることが示唆された[18]。

NHEの活性化はホルモン，機械刺激などで引き起こされる。筋ジス筋細胞におけるNHE活性化に寄与するいくつかの候補の中から，最近ATPが有力なメディエータになると考えられる以下の知見を得た[18]。①筋ジス筋細胞では，ATPの外液への遊離が未刺激時から確認され，伸展刺激によってさらにコントロールの2倍以上になることが分かった(図5C)。②ATP刺激でコントロール筋細胞ではNHE活性が上昇するが，筋ジス筋細胞ではNHEの恒常的活性化のためさらなる

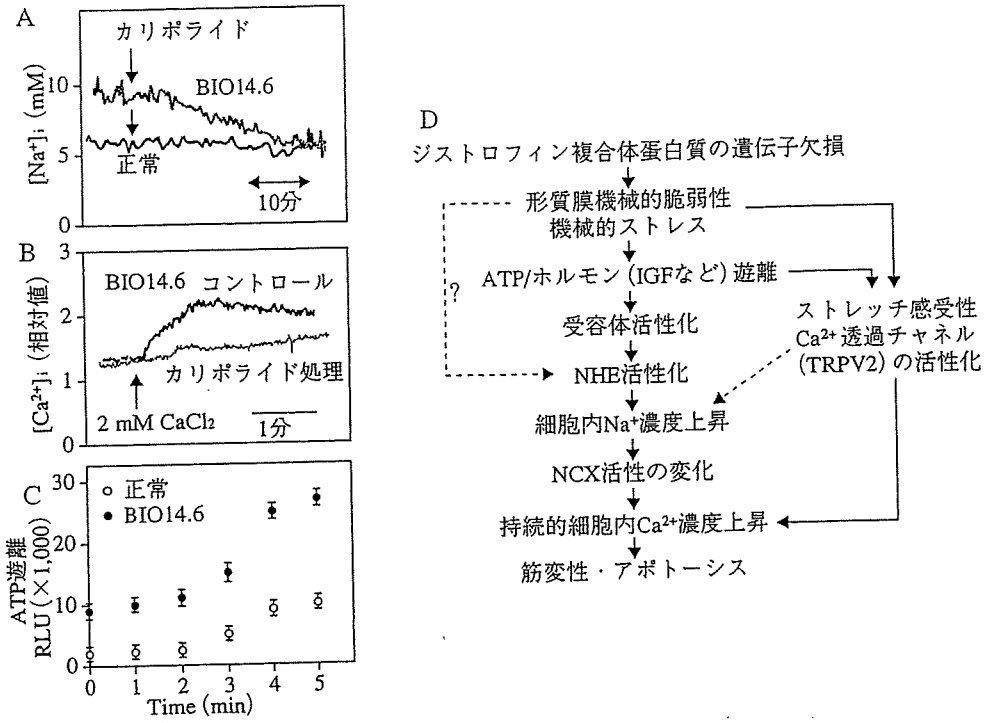

図5．筋ジスハムスター(BIO14.6)筋細胞を用いた筋変性の分子メカニズム
A：蛍光色素SBFIを用いて測定した$[Na^+]_i$はBIO14.6の細胞では高く，カリポライドで抑制される．
B：蛍光色素fluo4を用いて測定した$[Ca^{2+}]_i$．BIO14.6筋細胞では正常筋細胞では観察されない外液Ca^{2+}依存の$[Ca^{2+}]_i$上昇が見られるが，あらかじめカリポライド処理しておくとその$[Ca^{2+}]_i$上昇が抑制される．
C：シリコン膜に培養した正常およびBIO14.6筋細胞に10％伸展刺激を横軸に示す時間与えた時遊離されるATP量を測定．BIO14.6細胞からの著明なATP遊離がある．
D：現在考えられる筋ジスハムスター(BIO14.6)における筋変性発症に関わる細胞内メカニズム．*mdx*マウスも同様のメカニズムで筋変性が引き起こされる可能性がある．

上昇はなかった。③ATP分解酵素(アピラーゼ)およびP2受容体の阻害剤(PPADS，スラミン)処理により筋ジス筋細胞で上昇していたpH_iが減少し，ストレッチ刺激によるCK漏出も抑制された。④実際，BIO14.6および*mdx*両筋ジスモデルにおいて，P2受容体の阻害剤を投与したところ，NHE阻害剤と同等以上の筋変性改善効果が得られた。興味深いことに，NHEとP2受容体の阻害剤を併用すると，さらに相加的な改善効果が見られた。

以上の結果を踏まえて，細胞骨格系蛋白質の遺伝子欠損によって筋変性が生じるまでの細胞内経路をまとめてみた(図5D)。ジストロフィン関連の細胞骨格系の遺伝子異常でまず筋細胞膜が機械的に脆弱になり，ストレッチ刺激が入った状態になると考えられる。その増加したストレッチ刺激は，何らかのメカニズムでATP(あるいはIGFなどのホルモン)を遊離させ，受容体を介してNHEを活性化する。ストレッチが直接NHEを活性化する

可能性もある。いずれにせよ活性化されたNHEは$[Na^+]_i$を上昇させ，NCX関与で$[Ca^{2+}]_i$が上昇し筋変性を導く。他方，著者らは以前にストレッチ感受性Ca^{2+}透過チャネルTRPV2が筋変性に伴って活性化され，$[Ca^{2+}]_i$上昇に寄与することを報告した[19]。すなわち，TRPV2によるCa^{2+}流入系の亢進とNCXによるCa^{2+}排出系抑制の相乗効果が持続的な$[Ca^{2+}]_i$上昇に寄与することは疑いない。ジストロフィンあるいはサルコグリカンが欠損すると，骨格筋だけでなく心筋でも筋変性が起こり，移殖しか治療の手段がない拡張型心筋症を発症する。心筋症における筋変性も筋ジスの骨格筋で解析したようなメカニズムの関与が考えられ，現在，治療薬開発への応用を検討している。

おわりに

本稿では，NHEは疾病を悪化させるいわば“悪玉”トランスポータとして紹介したが，KOマウスのフェノタイプを見ても明らかなように生理的には重要な蛋白質である。NHE(NHE1アイソフォーム)遺伝子を欠損させると，生後まもなく歩行性運動失調症やてんかん性痙攣発作などの神経変性症状を呈し，離乳前に死亡するケースが多い。またKOマウス全身の成長は遅く，これはおそらくpH_iが細胞増殖に関わることと関係があるだろう。カリポライドなどのNHE阻害剤の心臓病患者を対象とした臨床評価では，必ずしも意図した効果は得られなかった。しかしNHEを完全に抑制することは，Na^+蓄積を阻害する一方で，酸排出という生理的に重要な機能をも抑制してしまうことになりかねない。したがって，NHEの基本的な機能を堅持しつつも，“NHEの活性化をブロックする薬”が有効かもしれない。そのためにはまず，NHE活性制御の分子メカニズムを解明することが先決で，その先に画期的な創薬が見えてくるに違いない。

§ 文 献

1) Wakabayashi S, Shigekawa M, Pouyssegur J : Molecular physiology of vertebrate Na^+/H^+ exchangers. Physiol Rev 1997;77:51-74.
2) Orlowski J, Grinstein S : Diversity of the mammalian sodium/proton exchanger SLC9 gene family. Pflugers Arch 2004;447:549-65.
3) Wakabayashi S, Fafournoux P, Sardet C, et al : The Na^+/H^+ antiporter cytoplasmic domain mediates growth factor signals and controls "H^+-sensing". Proc Natl Acad Sci USA 1992;89:2424-8.
4) Hisamitsu T, Ben Ammar Y, Nakamura TY, et al : Dimerization is crucial for the function of the Na^+/H^+ exchanger NHE1. Biochemistry 2006;45:13346-55.
5) Hisamitsu T, Pang T, Wakabayashi S, et al : Dimeric interaction between the cytoplasmic domains of the Na^+/H^+ exchanger NHE1 revealed by symmetrical intermolecular cross-linking and selective co-immunoprecipitation. Biochemistry 2004;43:11135-43.
6) Pang T, Hisamitsu T, Wakabayashi S, et al : Role of calcineurin B homologous protein in pH regulation by the Na^+/H^+ exchanger 1 : tightly bound Ca^{2+} ions as important structural elements. Biochemistry 2004;43:3628-36.
7) Pang T, Su X, Wakabayashi S, et al : Calcineurin homologous protein as an essential cofactor for Na^+/H^+ exchangers. J Biol Chem 2001;276:17367-72.
8) Pang T, Wakabayashi S, Shigekawa M : Expression of calcineurin B homologous protein 2 protects serum deprivation-induced cell death by serum-independent activation of Na^+/H^+ exchanger. J Biol Chem 2002;277:43771-7.
9) Ben Ammar Y, Takeda S, Hisamitsu T, et al : Crystal structure of CHP2 complexed with NHE1-cytosolic region and an implication for pH regulation. EMBO J 2006;25:2315-25.
10) Karmazyn M, Gan XT, Humphreys RA, et al : The myocardial Na^+-H^+ exchange : structure, regulation, and its role in heart disease. Circ Res 1999;85:777-86.
11) Karmazyn M, Sawyer M, Fliegel L : The Na^+/H^+ exchanger : a target for cardiac therapeutic intervention. Curr Drug Targets Cardiovasc Haematol Disord 2005;5:323-35.

12) Wang Y, Meyer JW, Ashraf M, et al : Mice with a null mutation in the NHE1 Na^+-H^+ exchanger are resistant to cardiac ischemia-reperfusion injury. Circ Res 2003;93:776-82.
13) Avkiran M, Marber MS : Na^+-H^+ exchange inhibitors for cardioprotective therapy : progress, problems and prospects. J Am Coll Cardiol 2002;39: 747-53.
14) Engelhardt S, Hein L, Keller U, et al : Inhibition of Na^+-H^+ exchange prevents hypertrophy, fibrosis, and heart failure in beta(1)-adrenergic receptor transgenic mice. Circ Res 2002;90:814-9.
15) Kilic A, Velic A, De Windt LJ, et al : Enhanced activity of the myocardial Na^+/H^+ exchanger NHE-1 contributes to cardiac remodeling in atrial natriuretic peptide receptor-deficient mice. Circulation 2005; 112:2307-17.
16) Heineke J, Molkentin JD : Regulation of cardiac hypertrophy by intracellular signalling pathways. Nat Rev Mol Cell Biol 2006;7:589-600.
17) Iwata Y, Katanosaka Y, Wakabayashi S, et al : Protective effects of Ca^{2+} handling drugs against abnormal Ca^{2+} homeostasis and cell damage in myopathic skeletal muscle cells. Biochem Pharmacol 2005;70: 740-51.
18) Iwata Y, Hisamitsu T, Wakabayashi S, et al : Enhanced Na^+/H^+ exchange activity contributes to the pathogenesis of muscular dystrophy via involvement of P2 receptors. Am J Pathol 2007, in press.
19) Iwata Y, Katanosaka Y, Shigekawa M, et al : A novel mechanism of myocyte degeneration involving the Ca^{2+}-permeable growth factor-regulated channel. J Cell Biol 2003;161:957-67.

FEBS Letters 581 (2007) 5859–5864

Crystal structure of RVV-X: An example of evolutionary gain of specificity by ADAM proteinases

Soichi Takeda*, Tomoko Igarashi, Hidezo Mori

Department of Cardiac Physiology, National Cardiovascular Center Research Institute, 5-7-1 Fujishiro-dai, Suita, Osaka 565-8565, Japan

Received 2 November 2007; revised 21 November 2007; accepted 21 November 2007

Available online 3 December 2007

Edited by Hans Eklund

Abstract **Russell's viper venom factor X activator (RVV-X) is a heterotrimeric metalloproteinase with a mammalian ADAM-like heavy chain and two lectin-like light chains. The crystal structure of RVV-X has been determined at 2.9 Å resolution and shows a hook-spanner-wrench-like architecture, in which the metalloproteinase/disintegrin region constitutes a hook, and the lectin-like domains constitute a handle. A 6.5 nm separation between the catalytic site and a putative exosite suggests a docking model for factor X. The structure provides a typical example of the molecular evolution of multi-subunit proteins and insights into the molecular basis of target recognition and proteolysis by ADAM/adamalysin/reprolysin proteinases.**

Keywords: Metalloproteinase; Disintegrin; ADAM; Factor X activator; Snake venom; Reprolysin

1. Introduction

Blood coagulation factor X is a serine proteinase and is one of the key components of the hemostatic system [1]. In circulation, factor X exists as a zymogen and is converted to an active form, factor Xa, by cleavage of a single peptide bond between Arg194 and Ile195. This removes the heavily glycosylated first 52 amino terminal residues (AP: active peptide) of the heavy chain, resulting in exposure of the active site. Factor Xa in turn converts prothrombin to thrombin, which ultimately leads to formation of hemostatic plugs.

Venom from Russell's viper, *Daboia russelli*, has been recognized for its potent coagulation activity. Russell's viper venom factor X activator (RVV-X) is a well-characterized metalloproteinase which specifically activates factor X by cleaving the same Arg-Ile bond in factor X that is cleaved by factors IXa and VIIa during physiological coagulation [2,3]. RVV-X belongs to the P-IV class of snake venom metalloproteinases [4] and consists of a heavy chain of 57,600 Da and two light chains of 19,400 and 16,400 Da, linked by disulfide bonds [2,5,6]. The 427-residue heavy chain contains the metalloproteinase (M)/disintegrin (D)/cysteine-rich (C) domains [4,7] that are shared by the (ADAM) (a disintegrin and metalloproteinase)/adamalysin/reprolysin family proteins. ADAMs are membrane-anchored glycoproteins that can proteolytically release cell-surface-protein ectodomains, including cell adhesion molecules, growth factor precursors and their receptors, and have been associated with numerous diseases including rheumatoid arthritis, Alzheimer's disease, heart disease, and cancer [8,9]. The light chains of RVV-X share amino acid sequence homology with mammalian C-type (Ca^{2+}-dependent) lectins and C-type lectin-like proteins (CLPs) isolated from various snake venoms [7,10]. RVV-X is one of the best examples of an exogenous activators used in coagulation research and has also been frequently used in diagnostic applications [2]. However, the molecular mechanism by which RVV-X recognizes and cleaves factor X is poorly understood, primarily due to the lack of three-dimensional structural information.

We recently determined the three-dimensional structure of the metalloproteinase/disintegrin/cysteine-rich (MDC) domains of ADAM/adamalysin/reprolysin family protein VAP1 and suggested a potential protein–protein interaction site that may function in specifying target proteins [11]. Among the family proteins, RVV-X is unique in having CLP domains within the molecule and a strict substrate specificity. To extend our understanding of the protein–protein interactions and target specificity of this family of proteins, we determined the crystal structure of RVV-X. Here, we report the crystal structure of RVV-X at 2.9 Å resolution and present a factor X docking model.

2. Materials and methods

RVV-X was purchased from Enzyme Research Laboratories Inc. and was further purified using a CM Hi-Trap column (GE healthcare Bio-Science Corp.) in the presence of GM6001 (*N*-[(2*R*)-2-(hydroxamidocarbonyllethyl)-4-methylpentanoyl]-L-tryptophan methylamide (CALBIOCHEM)). Crystals were obtained by the sitting drop vapor diffusion method. Droplets were prepared by mixing 1 μl of protein solution and 1 μl of reservoir solution (0.1 M calcium acetate, 0.1 M sodium cacodylate, 10% PEG8000, pH 6.5) supplemented with one fifth volume of 10% PEG3350 and were equilibrated against 1 ml of reservoir solution at 293 K, typically for one week. Crystals were soaked in reservoir solution supplemented with 15% MPD (2-methyl-2,4-pentandiol) prior to flash cryo-cooling under a stream of nitrogen gas at 100 K.

The diffraction data set was acquired using the SPring-8 beamline BL41XU at a wavelength of 1.0 Å at 100 K. The best crystal generated a data set with a 2.9 Å resolution (Table 1). The asymmetric unit contained one RVV-X molecule. The RVV-X structure was solved by the molecular replacement method using search models constructed from acutolysin-C (1QUA), catrocollastatin/VAP2B (2DW0), and fIX-bind-

*Corresponding author. Fax: +81 6 6872 7485.
E-mail address: stakeda@ri.ncvc.go.jp (S. Takeda).

Abbreviations: RVV-X, Russell's viper venom factor X activator; ADAM, a disintegrin and metalloproteinase; MDC, metalloproteinase/disintegrin/cysteine-rich; HVR, hyper-variable-region; PEG, polyethyleneglycol

0014-5793/$32.00
doi:10.1016/j.febslet.2007.11.062

Table 1
Data collection and refinement statistics

	Crystal 1
Data collection	
Space group	$P2_12_12_1$
Cell dimensions	
a, *b*, *c* (Å)	70.4, 91.7, 152.9
a, b, c (°)	90, 90, 90
Resolution (Å)	50–2.9 (3.0–2.9)
R_{merge}[a]	0.069 (0.212)
I/r *I*	17.0 (7.0)
Completeness (%)	96.4 (79.5)
Redundancy	6.3 (5.5)
Refinement	
Resolution (Å)	44.6–2.91 (3.0–2.91)
No. reflections	21482 (1661)
R_{work}[b]/R_{free}[c]	0.218/0.273
No. atoms	
Protein	5300
Zn^{2+}	1
Ca^{2+}	5
carbohydrate	106
GM6001	28
R.m.s deviations	
Bond lengths (Å)	0.0045
Bond angles (°)	1.12

Highest resolution shell is shown in parenthesis.
[a] $R_{merge} = \sum_{hkl} \sum_i |I_i(hkl) - \langle I(hlk)\rangle| / \sum_{hkl} \sum_i I_i(hkl)$, where $I_i(hkl)$ is the *i*th intensity measurement of reflection *hkl* and $\langle I(hlk)\rangle$ is its average.
[b] $R_{work} = \sum (|F_{obs}| - |F_{calc}|) / \sum |F_{obs}|$.
[c] R_{free} = *R*-value for a randomly selected subset (5%) of the data that were not used for minimization of the crystallographic residual.

ing protein (IX-bp, 1J34), for the M, C and CLP domains, respectively. The final model includes amino acid residues 7-422 of the heavy chain, 1-59 and 64-133 of light chain-A (LA) and 3-123 of light chain-B (LB), and was refined to a resolution of 2.9 Å (Table 1). The overall resolution is not particularly high when compared to those of the other snake venom protein structures, most likely due to the relatively high solvent content of the crystal (ff 60%) and the flexible modular architecture of the MDC domains [12]. However, well-determined structural models for most sub-domains generated the electron-density maps that enable us to build a reliable model. The overall B-factor is relatively high (average B-factor of the total protein atoms is 72.2 Å^2) and the electron-densities associated with the charged side-chains located on the molecular surface (61 aa corresponding to 9% of the total model of 672 aa) are not clearly observed, however, almost all of the side-chains inside the molecule are defined in the final electron-density maps (Fig. 1B and C). Details of preparation, crystallization and structural analysis are described in the Supplementary information.

3. Results and discussion

3.1. Overall structure of RVV-X

The overall structure of RVV-X resembles a hook-spanner-wrench configuration, where the major portion of the heavy chain forms a hook and the remaining heavy chain portion and the light chains form a handle (Fig. 1A). The backbone structure of the heavy chain is essentially the same as each monomer of VAP1 [11] and catrocollastain/VAP2B [12], with the exception of the sub-domain orientations (Fig. 1D and E). There are direct, but less-specific interactions between the M and C domains, most likely resulting from crystal packing forces, such that the entire RVV-X MDC domain forms a closed C-shape structure, unlike the open C-shaped structures of VAP1 and catrocollastain/VAP2B. The M domain of RVV-X has a flat elliptical shape with a core formed by a five-stranded β-sheet and five α-helices and contains the conserved Zn^{2+}-binding HEXXHXXGXXHD sequence (residues 145–156) and a "Met-tern" (Met169) bearing the typical structural features of the metzincin family of metalloproteinases [13]. RVV-X has a fourth disulfide bridge (Cys27-Cys63) (Fig. 1B), in addition to the three conserved disulfide bridges (Cys120-Cys200, Cys160-Cys184 and Cys162-Cys167) [4] in the M domain. The M domain is followed by the D and C domains, which are further divided into shoulder (D_s), arm (D_a), wrist (C_w) and hand (C_h), segments, and the entire heavy chain folds into a C-shaped structure (Fig. 1A). The heavy chain contains three structural Ca^{2+}-binding sites and a number of disulfide bridges (9 and 5 in the D and C domains, respectively) that are highly conserved among the ADAM/adamalysin/reprolysin family proteins [11,12].

The two homologous light chains have a fold similar to the carbohydrate-recognition domain (CRD) of rat mannose binding protein (MBP) [14], but they form an intertwined dimer where the central portion of each chain projects toward the adjoining subunit (Fig. 1A). The light chains are related by a pseudo 2-fold axis which is perpendicular to the long axis of the light chain dimer.

3.2. (HVR)-mediated protein–protein interaction

RVV-X has a unique cysteine residue (Cys389) in the middle of the hyper-variable-region (HVR, residues 373–394) in C_h, a putative protein–protein interaction site for this family of proteins [11]. Cys389 forms a disulfide bond with the C-terminal cysteine residue (Cys133) of LA (Fig. 1A and C). Aside from this inter-chain disulfide bridge, Tyr346, Tyr347, and Met385 in the heavy chain form multiple hydrophobic interactions and hydrogen bonds with Tyr11, Phe12, and Pro131 in LA, which further stabilize the continuous C_h/LA structure (Fig. 1C). Most of these residues involved in the interaction between C_h and LA are not conserved among ADAMs [11,12] or among other CLPs [10]. The RVV-X structure represents the first example of HVR-mediated protein–protein interactions by the ADAM/adamalysin/reprolysin family proteins.

3.3. Light chains

Both the overall structure and the surface features of the RVV-X light chains are quite similar to those of the factor X-binding protein (X-bp) from *Deinagkistrodon actus* venom (the r.m.s. deviation of the 240 equivalent Cα atoms is 2.6 Å) determined in complex with the γ-carboxyglutamic acid (Gla) domain of factor X [15] (Fig. 2A and B). X-bp has strong anticoagulant activities because it binds to the Gla domain of factor X and inhibits its membrane-anchoring function [16]. The hydrophobic residues that are critical for the membrane-anchoring function of factor X (Phe4, Leu5 and Val8) interact with the hydrophobic patch formed by the hydrophobic residues (Met113, Ile114 and Ala115) of the B chain in X-bp [15]. Those residues are conserved in RVV-X (Phe114, Ile115 and Ala116 of LB) (Fig. 2B). The positively charged patches on X-bp that directly interact with the Gla residues in factor X are conserved, but, are less prominent in RVV-X because of amino acid substitutions (especially, Ile101 and Glu104) (Fig. 2B). The structural similarities between the RVV-X light chains and X-bp suggest the intriguing possibility that RVV-X recognizes the factor X Gla domain through an exosite, formed by the light chains (Fig. 2C).

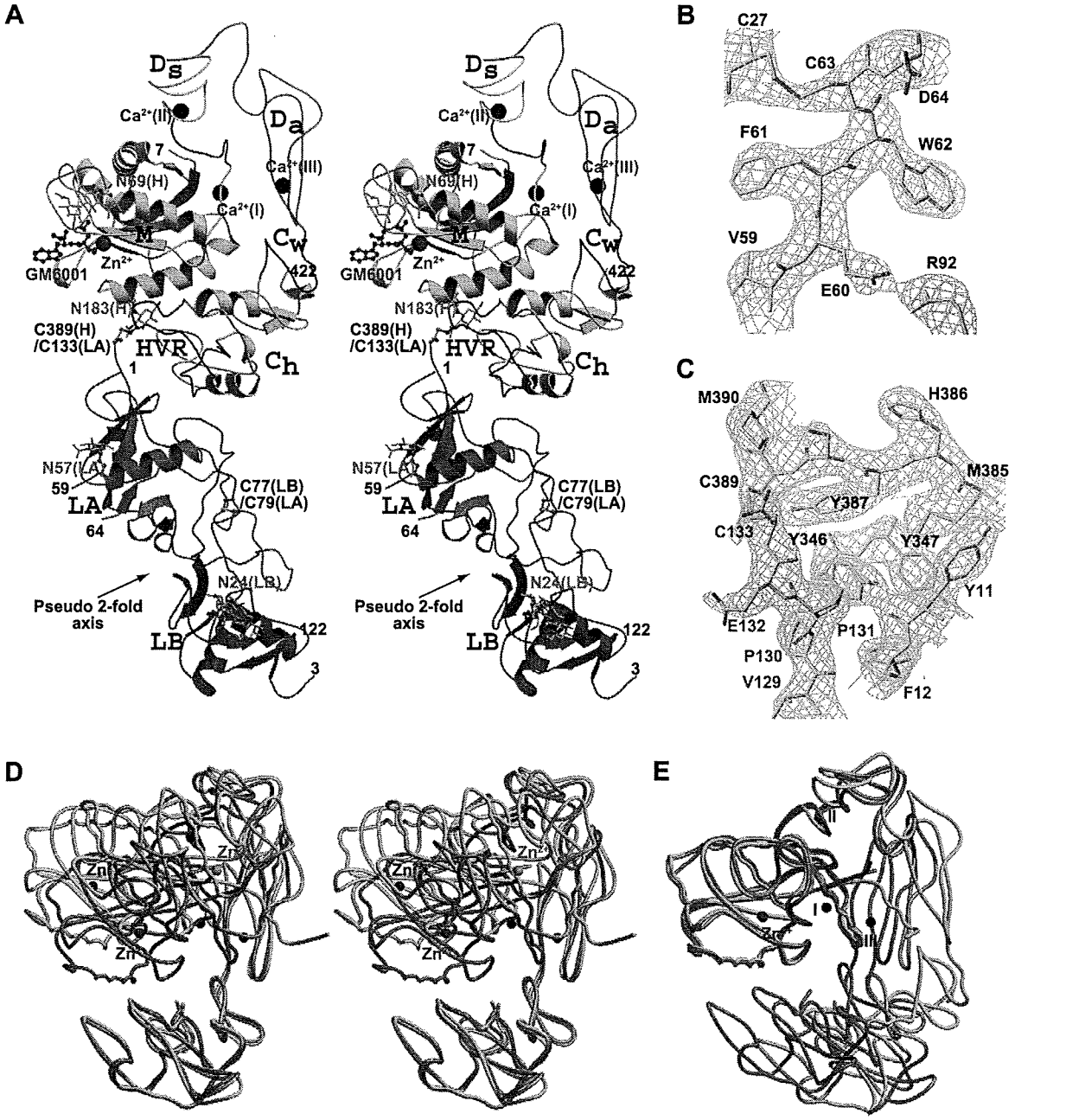

Fig. 1. Structure of RVV-X. (A) Ribbon structure of RVV-X in stereo. Bound calcium and zinc ions are represented by black and red spheres, respectively. The carbohydrate moieties (in green) linked to asparagine residues and GM6001 (in magenta) are shown in ball-and-stick representations. $2F_o$ F_c electron-density maps (1.0r) around the disulfide bridge between Cys27(HC) and Cys63(HC), and between Cys389 (HC) and Cys133 (LA) are represented in (B) and in (C), respectively. The HC and LA residues are labelled in black and in red, respectively. (D) Superimposition of the C_h segment of the RVV-X heavy chain (in pink) with that of the VAP1 monomer (chain-A in 2ERO, in yellow), and with that of the catrocollastatin/VAP2B (chain-A in 2DW0, in cyan) in stereo. The bound zinc and calcium atoms in RVV-X are shown as red and black spheres, respectively. The zinc atoms in VAP1 and catrocollastain/VAP2B are shown as green and blue spheres, respectively. (E) Superimposition of the M domain of the RVV-X heavy chain with the M domains of the VAP1 monomer and catrocollastatin/VAP2B.

When a properly folded Gla domain is absent from factor X, the rate of factor X activation by RVV-X is markedly diminished. In the acarboxy factor X, in which Gla formation has been blocked by a vitamin K antagonist [17] or the Des (1-44) factor X [18], factor X activation occurs at less than 1% of the rate of native factor X. Activation of factor X by RVV-X is dramatically enhanced by millimolar Ca^{2+}, which induces a conformational change in the Gla domain that enhances its binding to RVV-X [19]. Moreover, RVV-X catalyzed factor X activation is inhibited by X-bp [7]. Collectively, these observations suggest that the concave cleft created between the two light chains in RVV-X may function as an exosite for factor X-binding.

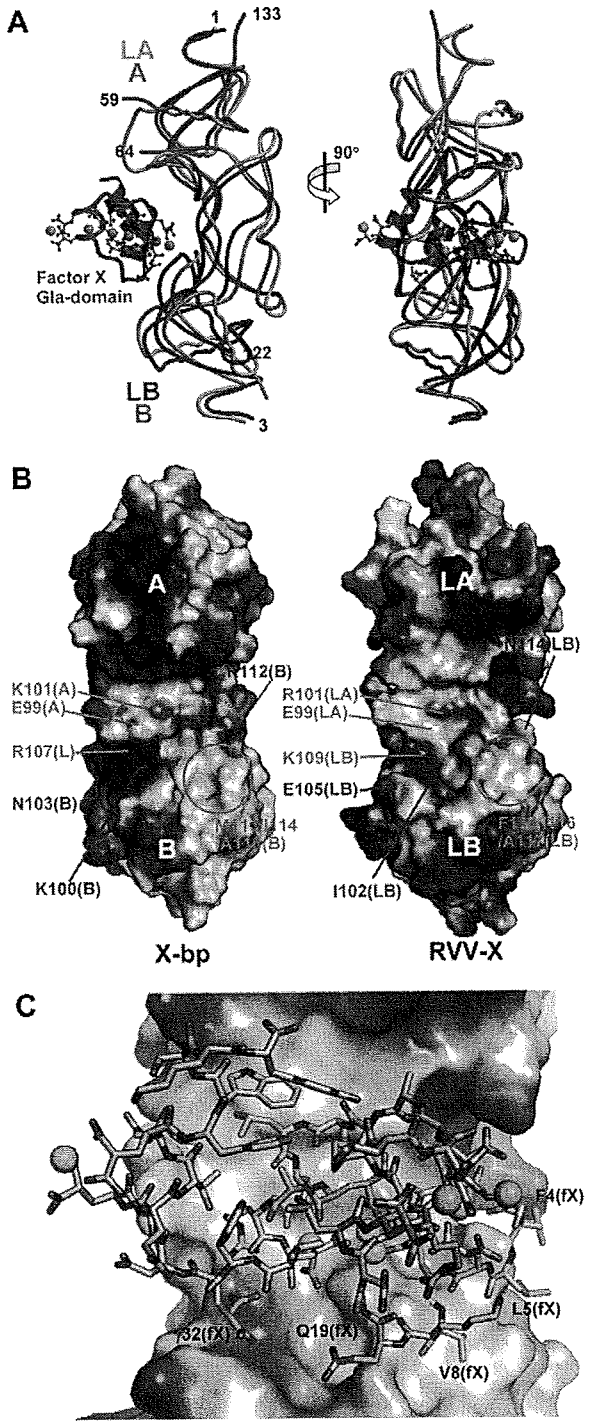

Fig. 2. Comparison of the RVV-X light chains and X-bp. (A) Superimposition of the RVV-X light chains (LA in orange and LB in magenta) onto the structure of X-bp (in gray) in complex with the Gla domain (in pink) of factor Xa (1IOD). The Gla residues and the Ca^{2+} ions are shown in ball-and-stick representation and as green spheres, respectively. (B) The molecular surfaces of X-bp and the light chains of RVV-X are represented according their electrochemical potentials (blue for positive, red for negative) and are viewed from the pseudo 2-fold axis. Conserved and varied residues are labelled in cyan and in red, respectively. (C) A model of the RVV-X light chains in complex with the Gla domain that was positioned based on the X-bp/fX Gla domain complex structure.

3.4. Docking model

Fig. 3A represents a preliminary docking model. For constructing a model, firstly, the second EGF domain (EGF2) and the serine proteinase (SP) domain of factor Xa (PDBID:1XKA) were placed such that the N-terminus of the factor X heavy chain (Ile195) closely approaches the RVV-X active site, and the globular SP domain fits into the concave

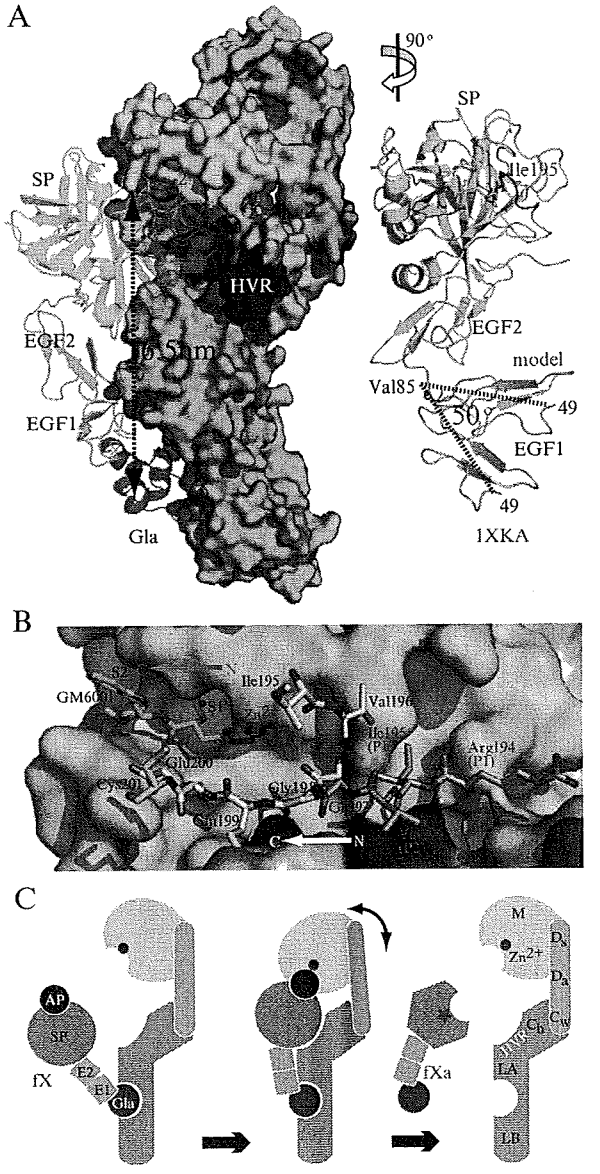

Fig. 3. Docking model. (A) The surfaces of the RVV-X sub-domains are coloured as in Fig. 1A. Factor Xa is shown in ribbon representation. Ile195 (in stick representation) and the N-terminal region (residues 195-201) of the factor X heavy chain are shown in magenta. In the right panel, the EGF1 segment of the original structural model (1XKA) is shown in gray. (B) Close up view of the RVV-X catalytic site of the docking model viewed from inside the factor Xa molecule. The N-terminal residues of factor Xa are shown in white and those of the model of factor X (zymogen) are shown in light pink. Because the factor X structure is currently unavailable, we assumed that this region has an extended structure. (C) Schematic model of factor X activation by RVV-X.

surface created by the C_h/LA domains. Secondly, we introduced a 50° bend between the two EGF domains so that the EGF1 domain fits to the convex surface of the LA domain (Fig. 3A). The linker between the two EGF domains is most likely flexible in solution [20]. This displacement successfully placed the N-terminus of the EGF1 domain in close proximity to the C-terminus of the Gla domain.

In the factor Xa structure, the N-terminal residue of the heavy chain, Ile195, is buried within the protein [20]. However, in the zymogen, the intact Arg194-Ile195-containing segment must be situated on the molecular surface, as in the equivalent segments of other serine proteinase zymogen structures [21]. The region of factor X that is C-terminal to the scissile peptide (segment coloured in magenta in Fig. 3A) may be located along the surface of the SP domain, resulting in its binding to the primed region of RVV-X, in the same orientation as the peptide-like inhibitor GM6001 lies in the current crystal structure (Fig. 3B). In the present docking model, since both molecules were positioned just as a rigid body without any collision, the active site zinc atom of RVV-X and Ile195 of factor Xa are 16 Å apart. Intrinsic hinge motions of the modular M/D_s/D_a/C_w architecture [12], and conformational changes upon association of RVV-X and the factor X zymogen, may allow the catalytic site of RVV-X to interact directly with the Arg194-Ile195 bond of factor X when in solution (Fig. 3C). The relatively large separation (ff65 Å) of the catalytic site and the Gla-domain-binding exosite may explain the high specificity of RVV-X for factor X.

3.5. Implication for molecular evolution of RVV-X

CLPs from snake venoms are characterized by a unique dimerization mechanism of protein evolution, in which two monomers swap a portion of the long loop region, forming a stable functional unit and creating a new concave surface for target binding for a variety of biological activities [10]. Dimers can further aggregate with each other to form higher-order oligomers [22], or, as in the case of RVV-X, form covalently linked complexes with a metalloproteinase chain creating an exosite. The RVV-X structure illustrates a good example of evolutionary gain of function by multi-subunit proteins, represented by the fold adaptation, for the binding of other ligands.

4. Conclusion

ADAMs are widely distributed and constitute the major membrane-bound sheddases to play roles in important processes occurring at the cell surface. However, the molecular mechanism of target recognition by ADAMs and which ADAMs shed which key substrates in specific biological events has been poorly understood. Previously, we suggested that the HVR may constitute an exosite that captures the target or associated proteins, and that is processed by the catalytic site [11]. The RVV-X structure is consistent with this model and provides insights into the molecular basis of HVR-mediated protein–protein interactions and target recognition by ADAM/adamalysin/reprolysin family proteins.

Acknowledgements: The authors thank M. Tomisako for help in crystallization experiments, M. Kawamoto and N. Shimizu for assistance with data acquisition at the SPring-8 beamline BL41XU and T. Morita for helpful discussions. This work was partly supported by the Ministry of Education, Science, Sports and Culture, Grant-in-aid for Scientific Research B-19370047-2007, and Health and Labor Science Research Grants, and by grants from the Mitsubishi Pharma Research Foundation and the Astellas Foundation for Research on Metabolic Disorders. T.I is supported by the grant from New Energy and Industrial Technology Development Organization (NEDO) of Japan.

Appendix A. Supplementary data

The atomic coordinates and structure factors have been deposited in the NCBI protein data bank with the accession code 2E3X. Supplementary data associated with this article can be found, in the online version, at doi:10.1016/j.febslet.2007.11.062.

References

[1] Mann, K.G., Nesheim, M.E., Church, W.R., Haley, P. and Krishnaswamy, S. (1990) Surface-dependent reactions of the vitamin K-dependent enzyme complexes. Blood 76, 1–16.
[2] Morita, T. (1998) Proteases which activate factor X in: Enzymes from Snake Venom (Bailey, G.S., Ed.), pp. 179–208, Alaken, Colorado.
[3] Tans, G. and Rosing, J. (2001) Snake venom activators of factor X: an overview. Haemostasis 31, 225–233.
[4] Fox, J.W. and Serrano, S.M. (2005) Structural considerations of the snake venom metalloproteinases, key members of the M12 reprolysin family of metalloproteinases. Toxicon 45, 969–985.
[5] Gowda, D.C., Jackson, C.M., Hensley, P. and Davidson, E.A. (1994) Factor X-activating glycoprotein of Russell's viper venom. Polypeptide composition and characterization of the carbohydrate moieties. J. Biol. Chem. 269, 10644–10650.
[6] Kisiel, W., Hermodson, M.A. and Davie, E.W. (1976) Factor X activating enzyme from Russell's viper venom: isolation and characterization. Biochemistry 15, 4901–4906.
[7] Takeya, H., Nishida, S., Miyata, T., Kawada, S., Saisaka, Y., Morita, T. and Iwanaga, S. (1992) Coagulation factor X activating enzyme from Russell's viper venom (RVV-X). A novel metalloproteinase with disintegrin (platelet aggregation inhibitor)-like and C-type lectin-like domains. J. Biol. Chem. 267, 14109–14117.
[8] White, J.M. (2003) ADAMs: modulators of cell–cell and cell–matrix interactions. Curr. Opin. Cell Biol. 15, 598–606.
[9] Seals, D.F. and Courtneidge, S.A. (2003) The ADAMs family of metalloproteases: multidomain proteins with multiple functions. Genes Dev. 17, 7–30.
[10] Morita, T. (2005) Structures and functions of snake venom CLPs (C-type lectin-like proteins) with anticoagulant-, procoagulant-, and platelet-modulating activities. Toxicon 45, 1099–1114.
[11] Takeda, S., Igarashi, T., Mori, H. and Araki, S. (2006) Crystal structures of VAP1 reveal ADAMs' MDC domain architecture and its unique C-shaped scaffold. EMBO J. 25, 2388–2396.
[12] Igarashi, T., Araki, S., Mori, H. and Takeda, S. (2007) Crystal structures of catrocollastatin/VAP2B reveal a dynamic, modular architecture of ADAM/adamalysin/reprolysin family proteins. FEBS Lett. 581, 2416–2422.
[13] Gomis-Ruth, F.X. (2003) Structural aspects of the metzincin clan of metalloendopeptidases. Mol. Biotechnol. 24, 157–202.
[14] Weis, W.I., Kahn, R., Fourme, R., Drickamer, K. and Hendrickson, W.A. (1991) Structure of the calcium-dependent lectin domain from a rat mannose-binding protein determined by MAD phasing. Science 254, 1608–1615.
[15] Mizuno, H., Fujimoto, Z., Atoda, H. and Morita, T. (2001) Crystal structure of an anticoagulant protein in complex with the Gla domain of factor X. Proc. Natl. Acad. Sci. USA 98, 7230–7234.
[16] Atoda, H., Ishikawa, M., Mizuno, H. and Morita, T. (1998) Coagulation factor X-binding protein from Deinagkistrodon acutus venom is a Gla domain-binding protein. Biochemistry 37, 17361–17370.

[17] Lindhout, M.J., Kop-Klaassen, B.H. and Hemker, H.C. (1978) Activation of decarboxyfactor X by a protein from Russell's viper venom. Purification and partial characterization of activated decarboxyfactor X. Biochim. Biophys. Acta 533, 327–341.
[18] Morita, T. and Jackson, C.M. (1986) Preparation and properties of derivatives of bovine factor X and factor Xa from which the gamma-carboxyglutamic acid containing domain has been removed. J. Biol. Chem. 261, 4015–4023.
[19] Skogen, W.F., Bushong, D.S., Johnson, A.E. and Cox, A.C. (1983) The role of the Gla domain in the activation of bovine coagulation factor X by the snake venom protein XCP. Biochem. Biophys. Res. Commun. 111, 14–20.
[20] Kamata, K., Kawamoto, H., Honma, T., Iwama, T. and Kim, S.H. (1998) Structural basis for chemical inhibition of human blood coagulation factor Xa. Proc. Natl. Acad. Sci. USA 95, 6630–6635.
[21] Freer, S.T., Kraut, J., Robertus, J.D., Wright, H.T. and Xuong, N.H. (1970) Chymotrypsinogen: 2.5-angstrom crystal structure, comparison with alpha-chymotrypsin, and implications for zymogen activation. Biochemistry 9, 1997–2009.
[22] Fukuda, K., Mizuno, H., Atoda, H. and Morita, T. (2000) Crystal structure of flavocetin-A, a platelet glycoprotein Ib-binding protein, reveals a novel cyclic tetramer of C-type lectin-like heterodimers. Biochemistry 39, 1915–1923.

Polymer Journal, Vol. 39, No. 10, pp. 1065–1070 (2007)

Synthesis of Sugar-Polysiloxane Hybrids Having Rigid Main-Chains and Formation of their Nano Aggregates

Koutarou BEPPU,[1] Yoshiro KANEKO,[1] Jun-ichi KADOKAWA,[1,†]
Hidezo MORI,[2] and Takehiro NISHIKAWA[2]

[1]*Department of Nano-structured & Advanced Materials, Graduate School of Science and Engineering, Kagoshima University, 1-21-40 Korimoto, Kagoshima 890-0065, Japan*
[2]*National Cardiovascular Center Research Institute, 5-7-1, Fujishirodai, Suita 565-8565, Japan*

(Received March 22, 2007; Accepted July 12, 2007; Published August 28, 2007)

ABSTRACT: We synthesized sugar-polysiloxane hybrids having rigid main-chains by reaction of sugar-lactones with amine-functionalized polysiloxane (**1**). Reaction of gluconolactone (**2**) with **1** was performed to obtain polysiloxane (**3**) having polyol moieties derived from glucose. This material has the regularly controlled higher-ordered structure in solid state such as the hexagonal phase. A hydrophilic sugar-polysiloxane hybrid (**5**) was prepared by reaction of lactobionolactone (**4**) with **1**. Furthermore, an amphiphilic sugar-polysiloxane hybrid (**8**) was synthesized by introduction of stearoyl groups in addition to sugar groups on the surface of **1**. The SEM image of the amphiphilic material **8** exhibited formation of nano aggregates having the particle diameters of *ca.* 50 nm in water.
[doi:10.1295/polymj.PJ2006268]
KEY WORDS Glycopolymer / Sugar-lactone / Polysiloxane / Amphiphilic / Hybrid / Nano Aggregate /

There has been a growing interest in sugar portions of the glycoproteins because of exhibiting to bind to carbohydrate-recognition proteins, toxins, viruses, and cells. It has been known that a molecular assembly formed from the sugar-residues in the living system expresses stronger recognition ability than that of a single sugar molecule. This, so-called multivalent or cluster effect, has become a principle in the design of artificial glycoconjugate ligands. Therefore, polymeric materials having such functional sugar-residues, *i.e.*, 'glycopolymer', have widely been investigated because these materials efficiently show the multivalent effect.[1] So far, a number of such glycopolymers have been synthesized, which are composed of various organic polymer main-chains combined with a variety of sugar side-chains.[2–6]

Inorganic polymers such as polysiloxanes have various of interesting properties, *e.g.*, high oxygen permeability, low toxicity, and biocompatibility, which are advantages as biomaterials. Therefore, sugar-polysiloxane hybrids would be expected to have a significant potential for biological applications. In previous study, synthesis of such sugar-inorganic hybrids, composed of polydimethylsiloxane main-chain has been reported.[7–10] Since the main-chain has relatively flexible nature, nanostructures of the hybrid materials have not been controlled well.

Based on the above viewpoints, we paid attention to amine-functionalized polysiloxanes[11,12] for the main-chain of new sugar-polysiloxane hybrids, which were prepared by sol-gel reaction of amine-functionalized organoalkoxysilanes in strong acid aqueous solutions. The materials have rigid structures and construct hexagonal phase in solid state, because their frameworks are Si-O-Si network structures derived from trifunctional organoalkoxysilane. Furthermore, the materials are soluble in water and have reactive amino groups on the surface. Their rigidity, solubility, and reactivity would be advantageous properties to controlling nanostructures and introduction of various functional groups on the surface, in addition to the general characteristics of the inorganic polymers.

In previous communication, we briefly reported simple preparation method for a rigid polysiloxane hybrid (**3**) having polyol moieties using the amine-functionalized polysiloxane (**1**) and gluconolactone (**2**) (Scheme 1).[13] Because the sugar lactones like **2** react with the amino groups without protection of the hydroxy groups, they are useful substrates for such the simple procedure to exclude multi-reaction steps. However, **2** was not suitable for preparation of materials containing the sugar substituents, because the ring-opened moieties like the side chain of **3** formed from **2** had no any sugar-residues. Therefore, we have been carrying out studies on the synthesis of sugar-functionalized polysiloxane hybrids using disaccharide-lactone such as lactobionolactone (**4**), because the existence of sugar-residues can be maintained in spite of opening the lactone ring of **4** by the reaction with **1**.

†To whom correspondence should be addressed (Tel: +81-99-285-7743, Fax: +81-99-285-3253, E-mail: kadokawa@eng.kagoshima-u.ac.jp).

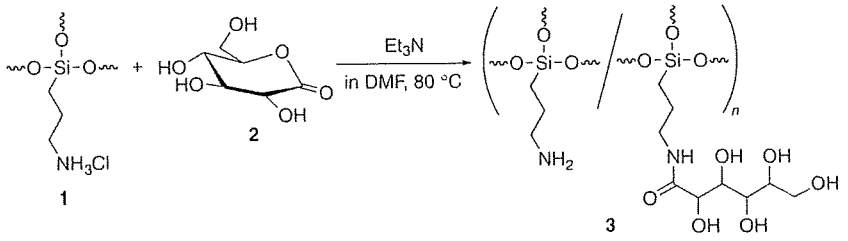

Scheme 1.

In this paper, we describe the synthesis of sugar-polysiloxane hybrids having rigid main-chains by the reaction of sugar-lactones with **1**. Furthermore, we prepared an amphiphilic sugar-polysiloxane hybrid by introduction of long alkyl chains in addition to sugar-residues on the surface of **1** to promote the formation of the nano aggregates in water, expecting the multivalent effects.

EXPERIMENTAL

Materials

The polysiloxane **1** was prepared according to the literature procedure.[11] *N,N*-Dimethylformamide (DMF), dimethyl sulfoxide (DMSO), and triethylamine were purified by distillation. Other reagents were used as received.

Reaction of 1 with Gluconolactone 2[13]

To a suspension of **1** (0.147 g, 1.0 mmol unit) in DMF (2.5 mL) was successively added triethylamine (0.15 mL, 1.1 mmol) and a solution of **2** (0.891 g, 5.0 mmol) in DMF (10 mL) with vigorously stirring at 80 °C under argon. After the mixture was stirred further at that temperature for 13 h, the obtained product was isolated by filtration, washed with DMF and acetone, and then dried under reduced pressure at 40 °C to yield 0.191 g of the yellow-powdered **3**. ^{1}H NMR (600 MHz, D_2O): δ 4.38–4.26 (br, -C(=O)-C*H*-), δ 4.16–4.05 (br, -C(=O)CH(OH)C*H*-), δ 3.88–3.60 (br, -C*H*(OH)C*H*(OH)CH_2-), δ 3.41–3.10 and 3.06–2.91 (br, -NCH_2-), δ 1.88–1.45 (br, -NCH$_2$CH_2-CH$_2$Si-), δ 0.94–0.47 (br, -CH_2Si-).

Synthesis of Hydrophilic Sugar-Polysiloxane Hybrid (5)

To a suspension of **1** (0.147 g, 1.0 mmol unit) in DMSO (3.0 mL) was successively added triethylamine (0.34 mL, 2.4 mmol) and a solution of **4** (1.701 g, 5.0 mmol) in DMSO (10 mL) with vigorously stirring at 80 °C under argon, and the mixture was stirred further at that temperature for 2 h. The mixture became gradually homogeneous solution. The solution was poured into acetone (300 mL) to precipitate the powdered product. The precipitated product was isolated by filtration, successively washed with acetone, hydrochloric acid (HCl) methanol solution and methanol, and then dried under reduced pressure at 40 °C to yield 0.332 g of the light yellow-powdered **5**. ^{1}H NMR (600 MHz, D_2O): δ 4.65–4.50 (br, -OC*H*-(CH-)O-), δ 4.50–4.32 (br, -C(=O)C*H*(OH)-), δ 4.32–4.13 (br, -C(=O)CH(OH)C*H*(OH)-), δ 4.08–3.49 (br, -C*H*(O-)C*H*(OH)CH_2OH, -C*H*(OH)C*H*(OH)C*H*(OH)-C*H*(O-)CH_2OH), δ 3.40–3.12 (br, -C(=O)NHCH_2-), δ 3.12–2.87 (br, Cl·NH$_3$CH_2-), δ 1.95–1.43 (br, -NCH$_2$CH_2CH$_2$Si-), δ 0.93–0.50 (br, -CH_2Si-).

Synthesis of Stearoyl-Carrying Polysiloxane (7)

To a solution of **1** (0.440 g, 3.0 mmol unit) in water (10 mL) was successively added triethylamine (1.0 mL, 7.2 mmol) and a solution of stearoyl chloride (**6**) (0.182 g, 0.6 mmol) in DMF (30 mL) with vigorously stirring at room temperature, and the solution was stirred further at that temperature for 10 min. After 5 mol/L HCl aqueous solution (2.88 mL, 14.4 mmol) was added to this mixture and this solution was stirred further for 5 min, the solution was poured into acetone (300 mL) to precipitate the powdered product. The precipitated product was isolated by filtration, washed with acetone and chloroform, and then dried under reduced pressure at 40 °C to yield 0.437 g of the white-powdered **7**. ^{1}H NMR (600 MHz, DMSO-d_6-D_2O): δ 3.09–2.72 (br, -NCH_2-), δ 2.20–2.01 (br, -C(=O)CH_2-), δ 1.88–1.55 (br, -NCH$_2$CH_2-CH$_2$Si-), δ 1.50–1.40 (br, -C(=O)CH$_2$CH_2-), δ 1.28–1.10 (br, -CCH_2C-), δ 0.95–0.45 (br, -CH$_3$, -CH_2Si-).

Synthesis of Amphiphilic Sugar-Polysiloxane Hybrid (8)

To a solution of **7** (0.150 g, 1.3 mmol unit) in DMSO (5 mL) was successively added triethylamine (0.46 mL, 3.3 mmol) and a solution of **4** (2.212 g, 6.5 mmol) in DMSO (15 mL) with stirring at 80 °C, and the solution was stirred further at that temperature for 2 h. The solution was poured into acetone (300 mL) to precipitate the powdered product. The precipitated product was isolated by filtration, successively washed with acetone, HCl methanol solution and

methanol, and then dried under reduced pressure at 40 °C to yield 0.270 g of the light yellow-powdered **8**. ^{1}H NMR (600 MHz, DMSO-d_6-D_2O): δ 4.46–4.28 (br, -OC*H*(CH-)O-), δ 4.28–4.11 (br, -C(=O)C*H*-(OH)-), δ 4.11–3.95 (br, -C(=O)CH(OH)C*H*(OH)-), δ 3.90–3.28 (br, -C*H*(O-)C*H*(OH)CH_2OH, -C*H*(OH)-C*H*(OH)C*H*(OH)C*H*(O-)CH_2OH, overlapped with HOD signal), δ 3.28–2.96 (br, -C(=O)NHCH_2-), δ 2.96–2.70 (br, Cl·NH_3CH_2-), δ 2.20–2.01 (br, -C(=O)-CH_2-), δ 1.80–1.32 (br, -NCH_2CH_2CH_2Si-, -C(=O)-CH_2CH_2-), δ 1.28–1.13 (br, -CCH_2C-), δ 0.88–0.80 (br, -CH_3), δ 0.80–0.36 (br, -CH_2Si-).

Measurements

The IR spectra were recorded using a SHIMADZU FT/IR-8400 spectrometer. The ^{1}H NMR spectra (600 MHz) were recorded using a JEOL ECA600 spectrometer. The gel permeation chromatographic (GPC) analyses were performed by using a TOSOH CCPD with RI detector under the following conditions: Shodex GF-310 column with water as the eluent at a flow rate of 0.5 mL/min. The calibration curve was obtained using pullulan standards. The X-ray diffraction (XRD) measurements were conducted at a scanning speed of $2\theta = 0.2°$/min using a RINT 1200 (Rigaku Co., Ltd) diffractometer with Ni-filtered CuKα radiation ($\lambda = 0.15418$ nm). The scanning electron microscope (SEM) images were obtained using a Hitachi S-4100 electron microscope. The dynamic light scattering (DLS) measurement was performed on a Zetasizer 3000 (Malvern Instruments).

RESULTS AND DISCUSSION

*Reaction of **1** with **2***

As previously reported,[13] an introduction of **2** to **1** was performed by heating at 80 °C in the presence of triethylamine in DMF to prepare a rigid polysiloxane **3** having polyol moieties (Scheme 1). The obtained product **3** was soluble in water and DMSO, but insoluble in typical organic solvents such as methanol, acetone, chloroform, and *n*-hexane.

The IR spectrum of the product showed an absorption at 1150 cm^{-1} attributed to the Si-O bond of the polysiloxane, an absorption at 1080 cm^{-1} assigned to the C-O bond of the polyol moiety derived from **2**, and an absorption at 1650 cm^{-1} due to the C=O bond of the amido group. In addition, the ^{1}H NMR spectrum in D_2O of the product showed both signals due to **1** and **2**. Furthermore, a methylene signal (δ 3.41–3.10) neighboring the amido group was appeared at lower magnetic field compared with a signal (δ 3.06–2.91) neighboring the unreacted amino group. These spectroscopic results indicated that the product has the structure **3** connecting **1** with **2** by the covalent bonds. The functionality of **2** to **1** was calculated to be *ca.* 75% based on the integrated ratio of the methylene signal neighboring the amido group to the methylene signal neighboring the silicon atom.

The molecular weights of **3** and **1** were evaluated by GPC analyses with water as the eluent. The GPC peak of **3** was shifted to the range of higher molecular weight compared to that of **1**. The M_n values of **3** and **1** estimated using pullulan standards were 21,200 g/mol ($M_w/M_n = 1.33$) and 10,300 g/mol ($M_w/M_n = 1.41$), respectively.

The XRD profile of **3** showed three peaks with the *d*-value ratio of $1:1/\sqrt{3}:1/2$ assigned to the (100), (110), and (200) peaks, respectively, indicating that the product has a hexagonal phase. Additionally, the *d*-value of the (100) peak of **3** ($d = 1.76$ nm) was larger than that of **1** ($d = 1.41$ nm). This indicates that the hexagonal phase in solid state was maintained in spite of the increase in the *d*-value by introduction of **2** to **1**.

The above analytical data indicated that **2** efficiently reacted with the amino groups in **1**, giving rise to **3**. To introduce the sugar moieties such as galactose residues on the surface of **1** by means of this reaction manner, the following experiments were performed using lactobionolactone **4**.

*Synthesis of Hydrophilic Sugar-Polysiloxane Hybrid **5***

We investigated synthesis of galactose-functionalized polysiloxane hybrid **5** by the reaction of **4** with **1**. Procedures for synthesis of **5** were almost same as those of **3**. Since the reaction in DMF gave the insoluble product, however, we employed DMSO as the alternative solvent, which was favorable for this reaction system. When an introduction of **4** to **1** was performed by heating at 80 °C in the presence of triethylamine in DMSO (Scheme 2), the initial reaction system was heterogeneous, which gradually became homogeneous with progress of the reaction. After the product was isolated as the fraction insoluble in acetone, unreacted amino groups were converted to ammonium cations by addition of HCl methanol solution in order to increase solubility and stability of the product in water. The obtained product **5** was soluble in water and DMSO, but insoluble in typical organic solvents such as methanol, acetone, chloroform, and *n*-hexane.

The IR spectrum of the product showed absorptions at 1650 cm^{-1} attributed to the C=O bond of the amido group, indicating the introduction of **4** to **1**. The ^{1}H NMR spectrum in D_2O of the product in Figure 1 shows both signals derived from **1** and **4**. Furthermore, a methylene signal $\mathbf{H_c}$ neighboring the amido group appeared at lower magnetic field compared with a signal $\mathbf{H_{c'}}$ neighboring the unreacted amino group. These spectroscopic data support the structure **5** of

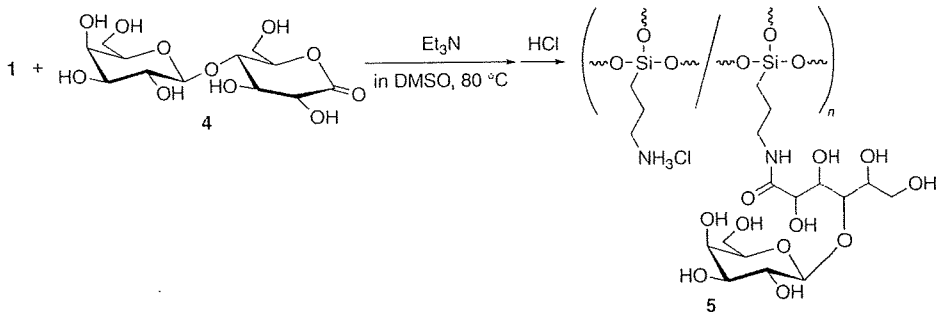

Scheme 2.

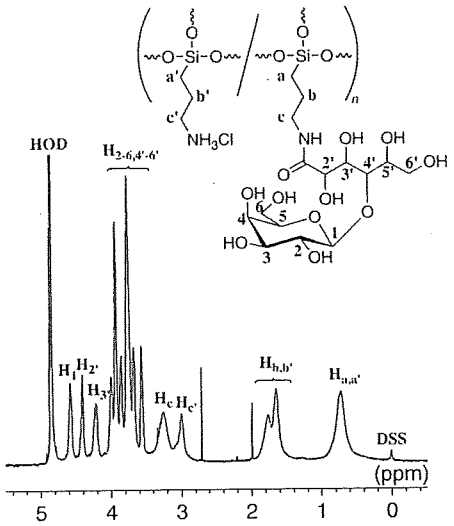

Figure 1. ^{1}H NMR spectrum of **5** in D_2O. Chemical shifts were referenced to sodium 2,2-dimethyl-2-silapentane-5-sulfonate (DSS) (δ 0.0 ppm).

the product. The functionality of **4** to **1** was calculated by the integrated ratio of the signal $\mathbf{H_1}$ to the signals $\mathbf{H_a}$ and $\mathbf{H_{a'}}$ in Figure 1 to be *ca.* 57%. Although the XRD profile of **3** showed three peaks for a typical hexagonal phase as described above, no diffraction peak was observed for **5**, indicating that a regular higher-ordered structure was not formed in the solid state. This would be because that the bulkiness of **4** affected the higher-ordered structure of **5**. However, **5** probably has the rigid structure in the solution due to the Si-O-Si network structure of the main-chain derived from trifunctional organoalkoxysilane. The molecular weight (M_n) of **5** estimated by GPC analysis with water as the eluent using pullulan standards was 44,700 g/mol (M_w/M_n = 1.44).

Synthesis of Amphiphilic Sugar-Polysiloxane Hybrid 8

To promote the formation of the nano aggregates of sugar-polysiloxane hybrid, we attempted synthesis of an amphiphilic hybrid **8** by introduction of the hydrophobic stearoyl groups in addition to the hydrophilic sugar groups on the surface of **5**. However, the reaction of **5** with stearoyl chloride **6** did not proceed to obtain **8**, probably due to bulkiness of sugar-residues existed on the surface of **5**. As an alternative reaction manner, an introduction of **6** to **1** was firstly carried out in the presence of triethylamine in water/DMF mixed solvent at room temperature to produce stearoyl-carrying polysiloxane **7** (Scheme 3). After addition of HCl aqueous solution to this reaction solution, the product was isolated as the fraction insoluble in acetone. The obtained product **7** was soluble in DMSO, but insoluble in water.

The IR spectrum of the product showed an absorption at 1640 cm^{-1} assigned to the C=O bond of the amido group. In addition, the ^{1}H NMR spectrum in DMSO-d_6 (including a small amount of D_2O) of the product in Figure 2 shows both signals derived from **1** and **6**. These spectroscopic results indicate the intro-

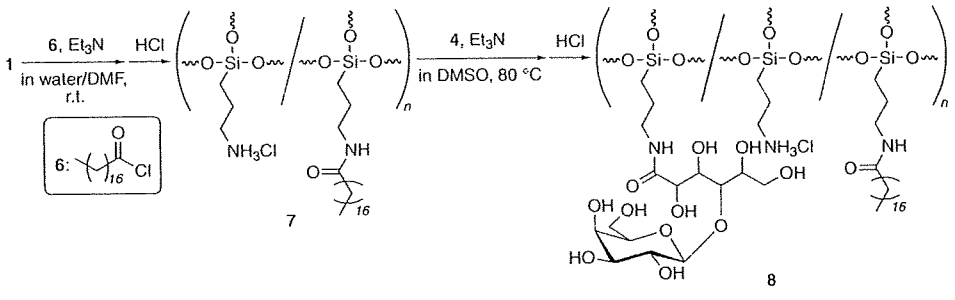

Scheme 3.

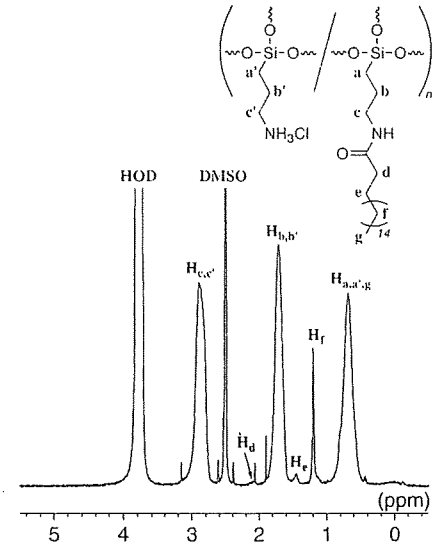

Figure 2. ^{1}H NMR spectrum of **7** in DMSO-d_6 (including a small amount of D_2O). Chemical shifts were referenced to DMSO (δ 2.5 ppm).

duction of **6** to **1**, leading to **7**. The functionality of **6** to **1** was calculated to be *ca.* 2% based on the integrated ratio of the signal $\mathbf{H_f}$ to the signal $\mathbf{H_b}$ and $\mathbf{H_{b'}}$. When the feed ratio of **6** to **1** was increased, the insoluble product was obtained.

As a second step, we carried out a reaction of **4** with **7** by heating at 80 °C in the presence of triethylamine in DMSO to obtain amphiphilic sugar-polysiloxane hybrid **8** (Scheme 3). The product was isolated as the fraction insoluble in acetone, followed by washing with acetone, HCl methanol solution, and methanol. The obtained product **8** was soluble in water and DMSO, but insoluble in typical organic solvents such as methanol, acetone, chloroform, and *n*-hexane.

The IR spectrum of the product showed an absorption at 1140 cm^{-1} attributed to the Si-O bond, an absorption at 1080 cm^{-1} assigned to the C-O bond of **4**, and an absorption at 1650 cm^{-1} due to the C=O bond of the amido group. Additionally, the ^{1}H NMR spectrum in DMSO-d_6 (including a small amount of D_2O) of the product in Figure 3a shows signals derived from **1**, **4**, and **6**. Furthermore, the methylene signals $\mathbf{H_a}$ and $\mathbf{H_b}$ of the product shift to higher field and the methylene signal $\mathbf{H_c}$ shifts to lower field compared with those of **7**. These shifts have also been observed in the synthesis of **3**,[13] and are attributed to progress of the amidation reaction of **7** with **4**. These spectroscopic results fully support the structure of the sugar- and stearoyl-functionalized polysiloxane **8**. The functionality of **4** to **1** was calculated by the integrated ratio of the signal $\mathbf{H_{f'}}$ to the signal $\mathbf{H_1}$ in Figure 3 to be *ca.* 48%, when the reaction was carried out under the conditions as described in experimental sec-

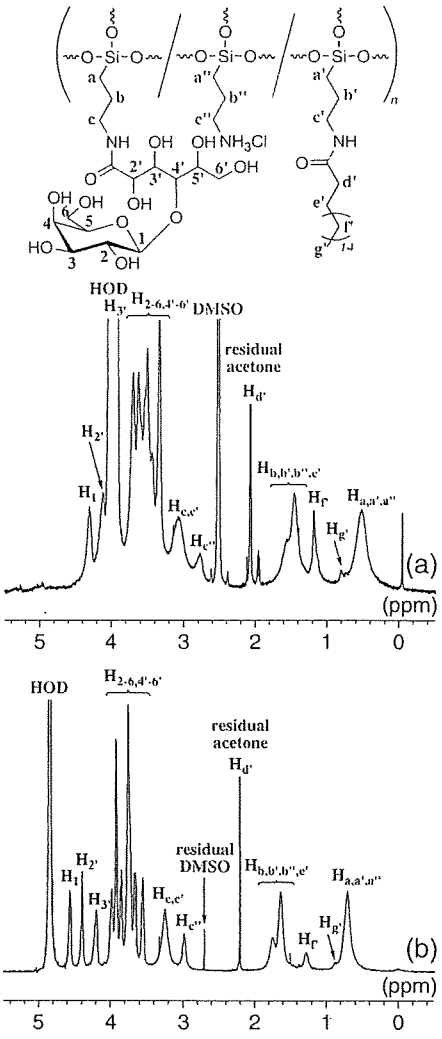

Figure 3. ^{1}H NMR spectrum of **8** (a) in DMSO-d_6 (including a small amount of D_2O) and (b) in D_2O. Chemical shifts were referenced to DMSO (δ 2.5 ppm) and DSS (δ 0.0 ppm), respectively.

tion. The functionalities were variable by changing the feed ratio of **4** to **7**.

Interestingly, intensity of a signal $\mathbf{H_{f'}}$ due to stearoyl group of **8** in D_2O decreases compared with that in DMSO-d_6 (Figure 3b). This observation indicates that the stearoyl groups existed in the inside of the intra and intermolecular aggregates of **8** in D_2O. To confirm the formation of nano aggregates of **8** in water, SEM image of **8** was taken. The SEM specimen was prepared by evaporating an aqueous solution of **8** on a spinning aluminium plate. The SEM image of the surface of **8** coated on the aluminum plate shows that nano aggregates were formed from **8** (Figure 4); nano aggregates having the particle diameters of *ca.* 50 nm are appearing at high frequency and larger particles that represent a diameter of *ca.* 500 nm are coexisting with smaller aggregates at much lower frequency (a few aggregates in a SEM image). The particle size

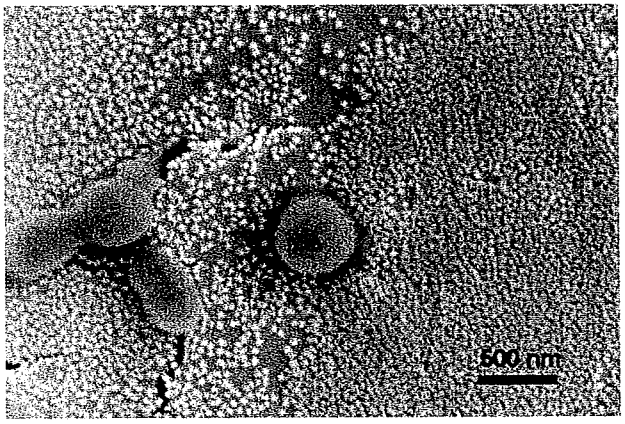

Figure 4. SEM image of **8**.

was also confirmed by dynamic light scattering (DLS) measurement. The mean diameter of the particle composed of **8** was 67.7 ± 4.5 nm (poly dispersity index: 0.273) in water. The aggregate size corresponds well to that was observed in the SEM image of the spin-coating sample of **8**.

CONCLUSIONS

The amino groups existed on the surface of the rigid polysiloxane (**1**) efficiently reacted with gluconolactone (**2**) to give the corresponding hybrid (**3**). This reaction manner was employed for preparation of the hydrophilic sugar-polysiloxane hybrid (**5**), which was achieved by the reaction of **1** with lactobionolactone (**4**). Furthermore, the amphiphilic sugar-polysiloxane hybrid (**8**) was also derived from **1** by the successive reactions with stearoyl chloride (**6**) and with **4**. The obtained hybrid materials **5** and **8** have galactose residues on their surfaces. Although hybrid **3** had the regular higher-ordered structure in the solid state, hydrophilic sugar-polysiloxane hybrid **5** did not form such a structure by the bulkiness of **4**. However, amphiphilic sugar-polysiloxane hybrid **8** formed the nano aggregates in water, which was confirmed by the ^{1}H NMR, SEM, and DLS analyses, expecting the multivalent effects of sugar-residues. The present materials are new class of sugar-inorganic hybrids, which have rigid polysiloxane main-chains.

Acknowledgment. The author (T.N.) thanks Dr. Tetsuji Yamaoka and Dr. Atsushi Mahara of National Cardiovascular Center for dynamic light scattering measurement.

REFERENCES

1. M. Okada, *Prog. Polym. Sci.*, **26**, 67 (2001).
2. K. Kobayashi, A. Tsuchida, T. Usui, and T. Akaike, *Macromolecules*, **30**, 2016 (1997).
3. X. L. Sun, K. M. Faucher, M. Houston, D. Grande, and E. L. Chaikof, *J. Am. Chem. Soc.*, **124**, 7258 (2002).
4. Q. Wang, J. S. Dordick, and R. J. Linhardt, *Chem. Mater.*, **14**, 3232 (2002).
5. A. B. Lowe, B. S. Sumerlin, and C. L. McCormick, *Polymer*, **44**, 6761 (2003).
6. L. Albertin, M. Stenzel, C. Barner-Kowollik, L. J. R. Foster, and T. P. Davis, *Macromolecules*, **37**, 7530 (2004).
7. G. Jonas and R. Stadler, *Acta. Polym.*, **45**, 14 (1994).
8. V. Braunmühl, G. Jonas, and R. Stadler, *Macromolecules*, **28**, 17 (1995).
9. V. Braunmühl and R. Stadler, *Polymer*, **39**, 1617 (1998).
10. K. Loos, G. Jonas, and R. Stadler, *Macromol. Chem. Phys.*, **202**, 3210 (2001).
11. Y. Kaneko, N. Iyi, K. Kurashima, T. Matsumoto, T. Fujita, and K. Kitamura, *Chem. Mater.*, **16**, 3417 (2004).
12. Y. Kaneko, N. Iyi, T. Matsumoto, and K. Kitamura, *Polymer*, **46**, 1828 (2005).
13. Y. Kaneko, J. Kadokawa, M. Setoguchi, and N. Iyi, *Polymer*, **46**, 8905 (2005).

ELSEVIER

Nutrition 23 (2007) 81–86

NUTRITION

www.elsevier.com/locate/nut

Basic nutritional investigation

Kurozu moromimatsu inhibits tumor growth of Lovo cells in a mouse model in vivo

Naoto Fukuyama, M.D., Ph.D.[a,*], Shio Jujo[a], Isao Ito, M.D., Ph.D.[b], Toru Shizuma, M.D., Ph.D.[a], Kazunori Myojin, M.D., Ph.D.[c], Kazuo Ishiwata, Ph.D.[a], Masanobu Nagano, Ph.D.[d], Hiroe Nakazawa, M.D., Ph.D.[a], and Hidezo Mori, M.D., Ph.D.[e]

[a] *Department of Physiology, Tokai University, School of Medicine, Isehara, Kanagawa, Japan*
[b] *Department of Surgery, Tokai University, School of Medicine, Isehara, Kanagawa, Japan*
[c] *Department of Radiology, Tokai University, School of Medicine, Isehara, Kanagawa, Japan*
[d] *Sakamoto Jozo Inc., Kagoshima, Kagoshima, Japan*
[e] *Department of Cardiac Physiology, National Cardiovascular Center, Suita, Osaka, Japan*

Manuscript received June 2, 2006; accepted October 12, 2006.

Abstract

Objective: In Japan, rice vinegar that has been matured and fermented for years in earthenware jars is considered a health food with anticolon cancer action. It is divided into the liquid component (Kurozu) and the sediment (Kurozu moromimatsu), which contains large amounts of organic materials and minerals. The effect of Kurozu moromimatsu (Kurozu-M) on cancer has not yet been examined. In this study, we examined the activity of Kurozu-M on colon cancer and investigated the mechanisms involved, focusing on active oxygen generation, apoptosis, and metalloproteinases (MMPs).

Methods: We used Lovo cells transplanted into nude mice as an experimental model. We measured the tumor volume and MMP levels and conducted hematoxylin-eosin staining (for polymorphonuclear leukocytes), terminal deoxynucleotidyl transferase-mediated dUTP nick end-labeling staining (for apoptosis), and immunostaining for nitrotyrosine (a marker of active oxygen generation) in control, Kurozu-treated, and Kurozu-M—treated groups.

Results: The tumor volume was the same in the control group (231 ± 36 mm^3) and Kurozu group (238 ± 52 mm^3), but was significantly reduced in the Kurozu-M group (152 ± 28 mm^3, $P < 0.001$ versus control). Apoptosis of tumor cells and accumulation of polymorphonuclear leukocytes were not observed. Nitrotyrosine production, total MMP levels, and MMP activation were significantly reduced in the Kurozu-M group.

Conclusion: The administration of Kurozu-M prolonged the lifespan of cancer cell–transplanted mice, inhibited tumor progression, and reduced nitrotyrosine production and MMP activation, but did not induce apoptosis.

Keywords: Kurozu; Kurozu moromimatsu; Lovo cell; Colon cancer

This work was supported by grants from Tokai University School of Medicine Research Aid in 2004, 2005, and 2006; the research and study program of Tokai University Educational System General Research Organization; the Kanagawa Nanbyou Foundation in 2004; Grants-in-Aid for Scientific Research in 2003 (grant 15659285), 2005 (grant 17659375), and 2006 (grant 18390336) from the Ministry of Education, Science and Culture, Japan; Health and Labour Sciences Research Grants for Research on Human Genome, Tissue Engineering Food Biotechnology in 2003 (grant H15-saisei-003); Health and Labour Sciences Research Grants for Comprehensive Research on Cardiovascular Diseases in 2004 (grant H16-jyunkannki[seishuu]-009) and 2006 (grant H18-jyunkannki[seishuu]-ippan-018); and Health and Labour Science Research Grants for research on medical devices for analyzing, supporting, and substituting the function of human body in 2005 (grant H17-physi-002).

* Corresponding author. Tel.: +81-463-931-121; fax: +81-463-936-684.
E-mail address: fukuyama@is.icc.u-tokai.ac.jp (N. Fukuyama).

0899-9007/07/$ – see front matter
doi:10.1016/j.nut.2006.10.004

Introduction

In Japan, rice vinegar is widely used in the preparation of Sushi or Kaisekiryouri. It is known to have a bactericidal action and an orexigenic action and was reported to have a preventive effect against hypertension and arterial sclerosis [1]. Recently, rice vinegar that has been matured and fermented for many years in earthenware jars has attracted attention as a health food. The supernatant is known as Korozu, and the solid residue of the production process, Kurozu moromimatsu (Kurozu-M), is rich in organic materials and minerals. However, the effect of Kurozu-M on disease has not yet been examined.

Colorectal cancer accounts for >90% of malignant tumors of the large intestine and is the third most common cause of death from malignant disease in the Western world [2]. It was reported that ethyl acetate extract of Kurozu inhibited carcinogenesis in azoxymethane-treated rats [3] and caused G0/G1 arrest through p21 induction in Caco-2 cells [4]. It is known that active oxygen species activate metalloproteinases (MMPs) in colon cancer tissue, leading to destruction of the basal membrane [5], thereby promoting distant metastasis. However, the effects of Kurozu on active oxygen production and MMP activation are unknown.

In this study, we examined the direct effects of Kurozu and Kurozu-M on human colon cancer cells (DLD cells, well-differentiated adenocarcinoma; Lovo cells, poorly differentiated adenocarcinoma) transplanted into nude mice and found that both inhibited tumor growth. We also examined the mechanisms involved, focusing on active oxygen production and MMP activation. Because direct measurement of active oxygen production in tissues is difficult, we used an indirect method based on staining for nitrotyrosine, the formation of which involves active oxygen.

Materials and methods

Preparation of Kurozu and Kurozu-M diets

The Kurozu and Kurozu-M diets were obtained from Sakamotojyozo Co., Ltd. (Kagoshima, Japan). The Kurozu diet included 0.32% 10-fold–concentrated Kurozu, and the Kurozu-M diet included 2% Kurozu moromimatsu powder in CE-2 basic rodent diet (Nihon CLEA Co., Ltd, Tokyo, Japan).

Preparation of animal model

Lovo and DLD cells were maintained under the conditions recommended by the supplier. Four-week-old to 6-wk-old female nude mice were maintained in a pathogen-free environment and handled according to the university's guidelines for animal care and use.

Female nu/nu mice were injected with 1×10^6 Lovo cells or DLD cells into the right flank. The tumors reached 5–10 mm in diameter at about 6 wk after injection in the control group on a standard CE-2 diet. The CE-2, Kurozu, or Kurozu-M diet was supplied from 1 wk before cancer cell injection.

Measurement of subcutaneous tumor

Tumor dimensions were measured with a linear caliper every 2 or 3 days for one month. We measured the major axis and the tumor volume, which was calculated using the equation $V\ (mm^3) = a \times b^2$, where a is the largest dimension and and b is the perpendicular diameter.

Hematoxylin-eosin staining, terminal deoxynucleotidyl transferase-mediated dUTP nick end-labeling staining, and nitrotyrosine immunostaining

At the end of the experiment, tumor tissue was fixed with 4% paraformaldehyde and sectioned. Hematoxylin-eosin (HE) staining was performed with conventional methods. Terminal deoxynucleotidyl transferase-mediated dUTP nick end-labeling (TUNEL) staining was performed according to the kit manufacturer's instructions, and apoptosis was visualized as brown staining, located in the nucleus. Apoptotic cells were counted in 10 fields of each slide under a 40× microscope.

For nitrotyrosine staining, endogenous peroxidase in sections was quenched with 0.3% H_2O_2 in 60% methanol for 30 min. The sections were permeabilized with 0.1% Triton X-100 in phosphate buffered saline (PBS) for 20 min. Nonspecific adsorption was minimized by incubating the sections in 2% normal goat serum in PBS for 20 min. Sections were incubated overnight with anti-nitrotyrosine rabbit polyclonal antibody (1:500 in PBS), and specific labeling was detected with diaminobenzidine tetrahydrochloride. To verify the binding specificity to nitrotyrosine, some sections were incubated with primary antibody only (no secondary antibody) or with secondary antibody only (no primary antibody). No positive staining was found in these sections, indicating that the immunoreaction was specific. Some sections were incubated with the primary antibody (anti-nitrotyrosine) in the presence of excess nitrotyrosine (10 mM) to further verify the binding specificity.

MMP-2 and MMP-9 assays

Levels of total MMP-2 and MMP-9 and endogenous activated MMP-2 and MMP-9 were assayed with commercial assay kits (Amersham Pharmacia Biotech, Buckinghamshire, UK).

MMP-2 assay

Eight weeks after injection of Lovo cells, tumors were removed. Tissues were homogenized in 50 mM Tris-HCl buffer (pH 7.4) containing 1 mM monothioglycerol and

centrifuged at 2000 *g* for 10 min. The supernatant was used as the sample. One hundred microliters of each standard blank or sample (in duplicate) was added to wells coated with MMP-2 antibody. The 96-well plate was then incubated overnight at 4°C. Any MMP-2 present within the samples was bound to the wells and other components were removed by washing. All standards and one well for each sample were activated with aminophenylmercuric acetate (APMA, 0.5 mM) to determine total MMP-2 levels, and the remaining wells were incubated with assay buffer alone to determine endogenous activated MMP-2. The detection reagent was then added to each well and the plate was incubated at 37°C for 4 h. After incubation, the absorbance of each well was read at 405 nm on a microplate reader and the concentrations (nanograms per milliliter) of total MMP-2 and endogenous activated MMP-2 were determined for each sample from a standard curve using Revelation Software (Dynatech, UK). Final tissue values were expressed as nanograms per milligram of protein.

MMP-9 assay

Standards and samples were run in the same manner as described for MMP-2 on a microplate coated with MMP-9 antibody, except that 1 mM APMA was used for activation, and incubation with the detection reagent was done at 37°C for 6 h. The absorbance was read with a microplate reader as described for MMP-2. Final tissue values were expressed as nanograms per milligram of protein.

Results

Measurement of subcutaneous tumor

We measured the major axis of the tumor to examine whether the administration of Kurozu or Kurozu-M could inhibit tumor growth. In the DLD cell–transplanted model, the major axes were 8.1 ± 0.5 mm in the control group, 7.90 ± 0.80 mm in Kurozu group, and 7.8 ± 0.80 mm in the Kurozu-M group. There were no significant differences among the three groups (Fig. 1A). However, in the Lovo cell–transplanted model, the major axes of the tumor were 8.2 ± 0.5 mm in the control group and 7.8 ± 0.8 mm in the Kurozu group, but significantly reduced to 6.0 ± 0.8 mm in the Kurozu-M group ($P < 0.05$ versus control; Fig. 1B).

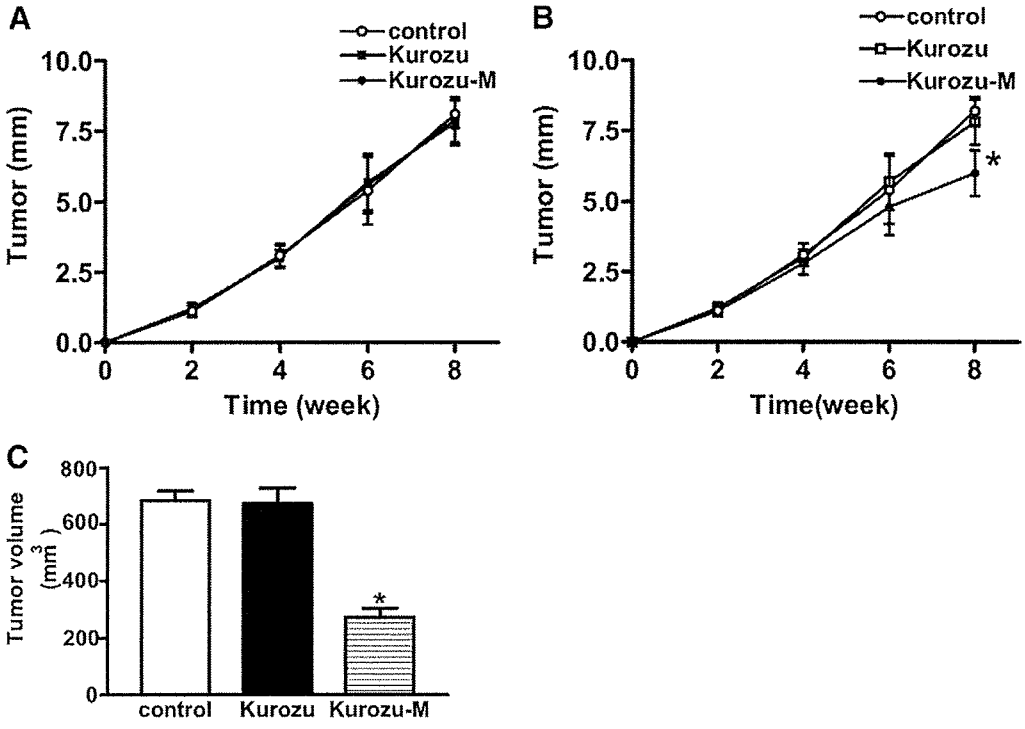

Fig. 1. Antitumor effect of Kurozu and Kurozu moromimatsu. Female nu/nu mice were injected with 1×10^6 Lovo cells or DLD cells into the right flank. (A) Time course of tumor growth in DLD-1 cell–transplanted mice (long diameter). Open circles represent the control group, solid squares the Kurozu-treated group, and solid circles the Kurozu moromimatsu–treated group. (B) Time course of tumor growth in Lovo cell–transplanted mice (long diameter). Open circles indicate the control group, open squares the Kurozu-treated group, and solid circles the Kurozu moromimatsu–treated group. (C) Tumor volume in Lovo cell–transplanted mice. Tumor volume was measured 8 wk after Lovo cell inoculation. The open bar indicates the control group, the solid bar the Kurozu-treated group, and the horizontally lined bar the Kurozu moromimatsu–treated group. Values are means ± SD. *$P < 0.001$ versus other groups.

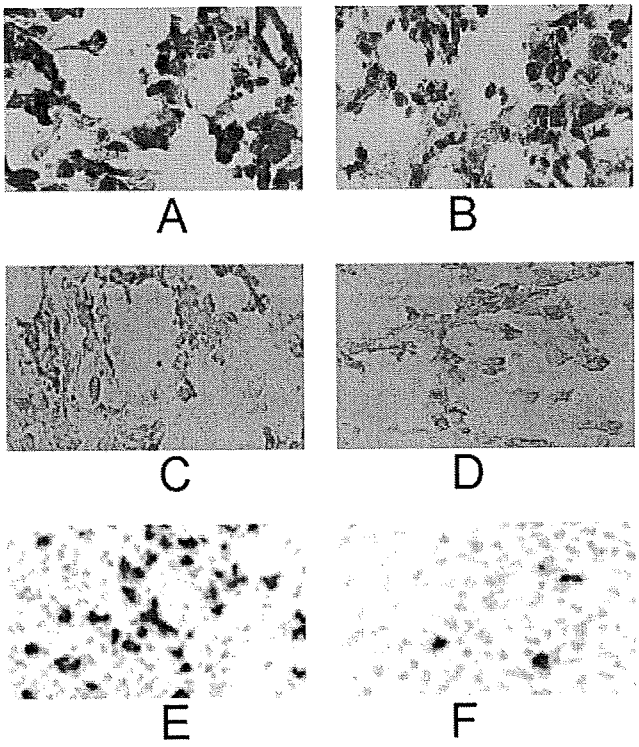

Fig. 2. Histologic examination of cancerous tissue after Lovo cell transplantation. Hematoxylin-eosin staining of tumor from (A) the control group and (B) the Kurozu moromimatsu–treated group. Terminal deoxynucleotidyl transferase-mediated dUTP nick end-labeling staining of tumor from (C) the control group and the (D) Kurozu moromimatsu–treated group. Nitrotyrosine staining of tumor from (E) the control group and (F) the Kurozu moromimatsu–treated group.

In the Lovo cell–transplanted model, the tumor volumes were 684.0 ± 34.0 mm^3 in the control group, 672.0 ± 56.0 mm^3 in the Kurozu group, and 273.0 ± 32.0 mm^3 in the Kurozu-M group ($P < 0.005$ for the Kurozu-M group versus control; Fig. 1C).

The following results refer to the Lovo cell–transplanted model.

HE staining, TUNEL staining, and nitrotyrosine immunostaining

The HE staining showed no accumulation of polymorphonuclear leukocytes, which have been implicated in active oxygen production, in tumor tissue in the control group or the Kurozu-M group (Fig. 2A,B).

The TUNEL staining indicated that apoptosis in the Kurozu-M group was at the same level as that in the control group (Fig. 2C,D).

Because we previously found that nitrotyrosine, generated from peroxynitrite and tyrosine, is produced in human colon cancer [5], we examined whether the administration of Kurozu-M could inhibit nitrotyrosine formation. In the control group, many cells produced nitrotyrosine, whereas in the Kurozu-M group, only a few cells produced nitrotyrosine (Fig. 2E,F).

MMP-2 and MMP-9 assays

To investigate the role of MMPs in the action of Kurozu-M, we examined whether or not Kurozu-M altered the levels and activation of MMPs.

Total MMP-2 amounted to 8.8 ± 2.5 ng/mg of protein in the control group and 8.6 ± 2.8 ng/mg of protein in the Kurozu group. However, it was significantly reduced to 5.6 ± 1.8 ng/mg of protein by administration of Kurozu-M ($P < 0.05$ versus control; Fig. 3A). Activated MMP-2 amounted to 0.25 ± 0.06 ng/mg of protein in the control group, 0.27 ± 0.08 ng/mg of protein in the Kurozu group, and 0.12 ± 0.05 ng/mg of protein in the Kurozu-M group ($P < 0.05$ for the Kurozu-M group versus control; Fig. 3A).

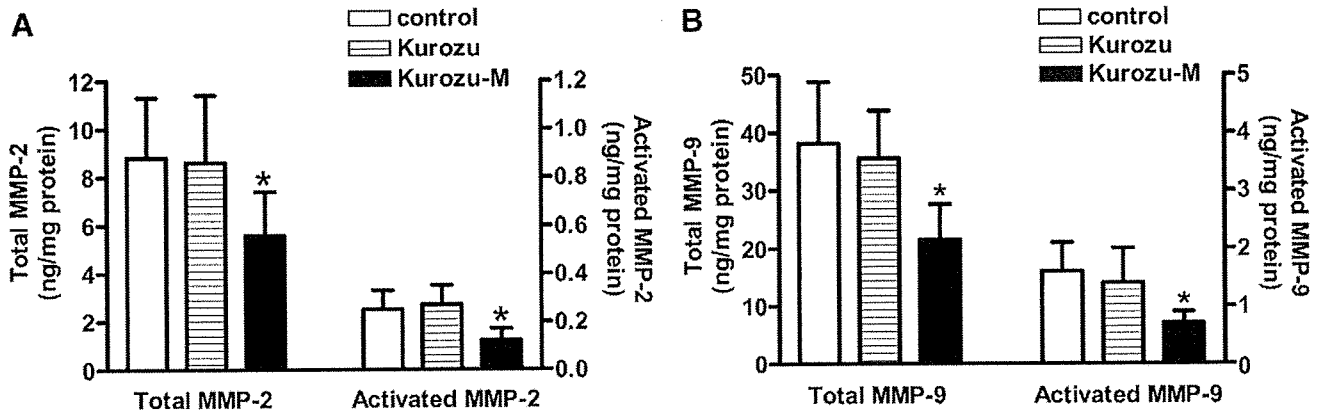

Fig. 3. Anti-metalloproteinase effect of Kurozu and Kurozu moromimatsu. (A) Total and activated metalloproteinase-2 in cancerous tissue after Lovo cell inoculation. The open bar represents the control group, the horizontally lined bar the Kurozu-treated group, and the solid bar the Kurozu moromimatsu-treated group. (B) Levels of total and activated metalloproteinase-9 in cancerous tissue after Lovo cell inoculation. The open bar represents the control group, the horizontally lined bar the Kurozu-treated group, and the solid bar the Kurozu moromimatsu–treated group.Values are means ± SD. $^*P < 0.001$ versus other groups.